

Dark Field Transmission Electron Microscopy as a Tool for Identifying Inorganic Nanoparticles in Biological Matrices

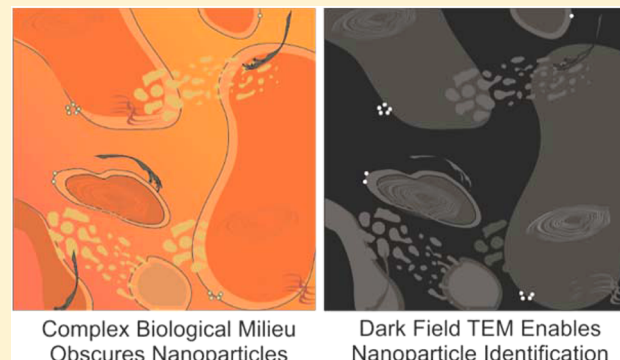
Nathan D. Klein,^{†,||} Katie R. Hurley,^{†,||} Z. Vivian Feng,[‡] and Christy L. Haynes*,[†]

[†]University of Minnesota, Department of Chemistry, 207 Pleasant St. SE, Minneapolis, Minnesota 55455, United States

[‡]Augsburg College, Department of Chemistry, 2211 Riverside Ave., Minneapolis, Minnesota 55454, United States

Supporting Information

ABSTRACT: Dark field transmission electron microscopy has been applied herein to visualize the interactions of inorganic nanomaterials with biological systems. This new application of a known technique addresses a deficiency in status quo visualization techniques. High resolution and low noise images can be acquired to locate and identify crystalline nanoparticles in complex biological matrices. Moreover, through the composition of multiple images taken at different angular beam tilts, it is possible to image a majority of nanoparticles present at a site in dark field mode. This facilitates clarity regarding the internalization of nanomaterials in cellular systems. In addition, comparing dark field images recorded at different angular tilts yields insight into the character of nanoparticle faceting.



As nanotechnology continues to become more and more prevalent, there is an increasing need to accurately characterize the interactions between nanomaterials and biological systems. The state and localization of nanomaterials inside cells and tissues are important considerations for intentional exposure (nanomedicine) and incidental exposure (nanotoxicology).^{1,2} Historically, the characterization of nanomaterials in biological systems has been made difficult due to the need for high resolution and the complexity of biological matrices, which include a milieu of proteins, lipids, high salinity conditions, etc. Although less often discussed, the low incidence of nanoparticles in many situations is another challenge for accurate characterization. For example, in studies of ecological nanotoxicity, relevant exposure concentrations may be at the ppm level or lower.³ High resolution techniques such as transmission electron microscopy (TEM) necessarily cover a small subset of each sample; thus, the probability of even finding a nanoparticle for characterization becomes very low.

Multiple techniques have been developed to allow for imaging of nanoparticles in biological matrices. Table 1 provides a sampling of the most common microscopy techniques for the visualization specifically of inorganic nanoparticles, including their prominent advantages and disadvantages. Although innovative techniques involving confocal Raman mapping,^{4–6} atomic force microscopy,^{7–11} and magnetic force microscopy^{12,13} have been used, TEM and fluorescence microscopy are by far the most common. In particular, TEM is valuable because of the extremely high resolution (<1 nm depending on experimental parameters) that allows for visualization of nanoparticle localization in cellular compartments as well as an accurate assessment of the

nanoparticle state (aggregation, shape change, etc.). In recent literature, two modes of TEM have been used to characterize nanoparticles in biological matrices: bright field and high angle annular dark field scanning transmission electron microscopy (HAADF-STEM). Bright field mode is the traditional imaging mode for TEM wherein electrons that are transmitted through the sample without much deflection are used to construct the image. This mode allows for nm-scale detail and visualization of the entire biological milieu surrounding the nanoparticles,^{14,15} however, most inorganic nanoparticles with high mass and crystallinity will appear dark in bright field mode, which means that researchers have to hunt for negative signal in a complex image. Heavy metal staining and other high density cell structures such as ribosomes can easily be mistaken for nanoparticles due to their similar size ranges and apparent contrast.¹⁶ The other imaging mode, HAADF-STEM, makes use of an annular detector to image only highly scattered electrons passing through the sample. This method, which is similar to dark field light microscopy, decreases the noise in the image and results in strong bright signal for high mass materials such as nanoparticles. The decrease in noise has led to elegant images by Morones et al. and others;^{17–20} however, most HAADF detectors are located such that they detect electrons scattered by mass and not by crystallinity. Because inorganic nanoparticles are often crystalline and biological matrices are not, this method can still yield similar contrast for the nanoparticle-containing cell or tissue, especially when high-

Received: January 10, 2015

Accepted: April 1, 2015

Published: April 1, 2015

Table 1. Comparison of Techniques for Visualizing Inorganic Nanoparticles in Biological Matrices

technique	description	advantages	disadvantages	reference
dark field transmission electron microscopy	image scattered electrons from mass and diffraction	high resolution, crystallinity-dependent contrast, low noise images	fixed sample, ^a labor-intensive sample preparation	current article
bright field transmission electron microscopy	image transmitted electrons	high resolution, mass- and crystallinity-dependent contrast, potential for elemental analysis (EDX) ^b	fixed sample, ^a labor-intensive sample preparation	14, 15, and 24
high angle annular dark field scanning transmission electron microscopy	image scattered electrons from high mass labeled cell structures	high resolution, mass-dependent contrast, low noise, potential for elemental analysis (EDX, EELS) ^b	fixed sample, ^a labor-intensive sample preparation, no crystallinity information	17–20 and 25–27
fluorescence microscopy	image fluorescence from nanoparticles and labeled cell structures	various fluorophores stain different cellular structures, live cell imaging, 3D information	resolution >200 nm (excepting super resolution techniques), cells must be stained	28 and 29
dark field light microscopy	image scattered visible light from cell and/or nanoparticle structures	lower noise than bright field light microscopy, does not require stain or labeling	resolution >200 nm, poor scattering from biological samples	28 and 29

^aIn specialized liquid flow cells or *in situ* TEM setups, biological samples do not necessarily require fixation.³⁰ ^bEDX (energy dispersive X-ray spectroscopy) and EELS (electron energy loss spectroscopy).

mass cellular components are present (consider for example the calcium precipitations present in the gut mitochondria of various species).^{21–23} In cases where nanoparticles are sparse and researchers are quickly scanning a sample, this method may not be helpful for finding or identifying crystalline nanoparticles. In addition, HAADF detectors are used in combination with STEM imaging, which is only available on specialized high resolution TEM instruments.

A third TEM mode, dark field mode, is available on typical TEM instruments with or without STEM capabilities. A schematic comparison between this technique, bright field TEM, and HAADF-STEM can be found in Figure 1. One of the main differences among these techniques is which electron population is used to construct the resultant image. As discussed previously, the beam of transmitted electrons is imaged in bright field mode. In this case, the objective aperture is often used to increase contrast by blocking scattered electrons. High mass or crystalline materials thus appear even darker when the aperture is inserted. In contrast, in traditional dark field mode, the incident beam of electrons is tilted at an angle (*d*) to the sample, and the electrons that scatter at a similar angle proceed down the center of the microscope column. Meanwhile, the transmitted electrons continue at an angle that is blocked by the objective aperture. The incident beam can be tilted both radially and angularly. A higher radial beam tilt corresponds to a higher scattering angle that is being imaged. The angular beam tilt corresponds to the direction of the diffraction, and thus, the orientation of the diffraction source. HAADF-STEM imaging requires a specialized annular detector to acquire the signal from highly scattered electrons. Due to its circular nature, the HAADF detector can gather electrons scattered in every direction simultaneously. At a high scattering angle, the signal intensity is correlated to the atomic number of the material being imaged. This means that a densely packed or high-mass but noncrystalline area could display the same contrast as a high-mass area with high crystallinity. The unique contrast from diffraction alone is minimized.

To our knowledge, dark field mode has not been previously utilized for the identification of inorganic nanoparticles in biological matrices, but it does provide several benefits over bright field and HAADF-STEM modes. This work demonstrates the benefits of dark field mode for identifying and characterizing inorganic crystalline nanoparticles in a variety of biological matrices. Dark field mode reduces visual noise but allows bright crystalline contrast for easy identification of nanoparticles in low-concentration samples. In addition, the crystalline contrast can be used to clearly differentiate stain or cell features from nanoparticles. Finally, the sequential mode of image acquisition described below will allow for enhanced nanoparticle study beyond studies in biological matrices by visualization of different crystal facets.

EXPERIMENTAL SECTION

Materials. Iron oxide nanoparticles (IONPs) were purchased as EMG-308 Ferrofluid from Ferrotec (Santa Clara, CA). Gold nanoparticles (Au NPs, 60 nm diameter) were purchased from Cabot Security Materials Inc. (Mountain View, CA). Au NPs (4 nm diameter) wrapped with poly(allylamine hydrochloride) were graciously provided by the Murphy group at the University of Illinois.

TEM Imaging. All transmission electron microscopy was done using an FEI Tecnai T12 microscope at 120 kV.

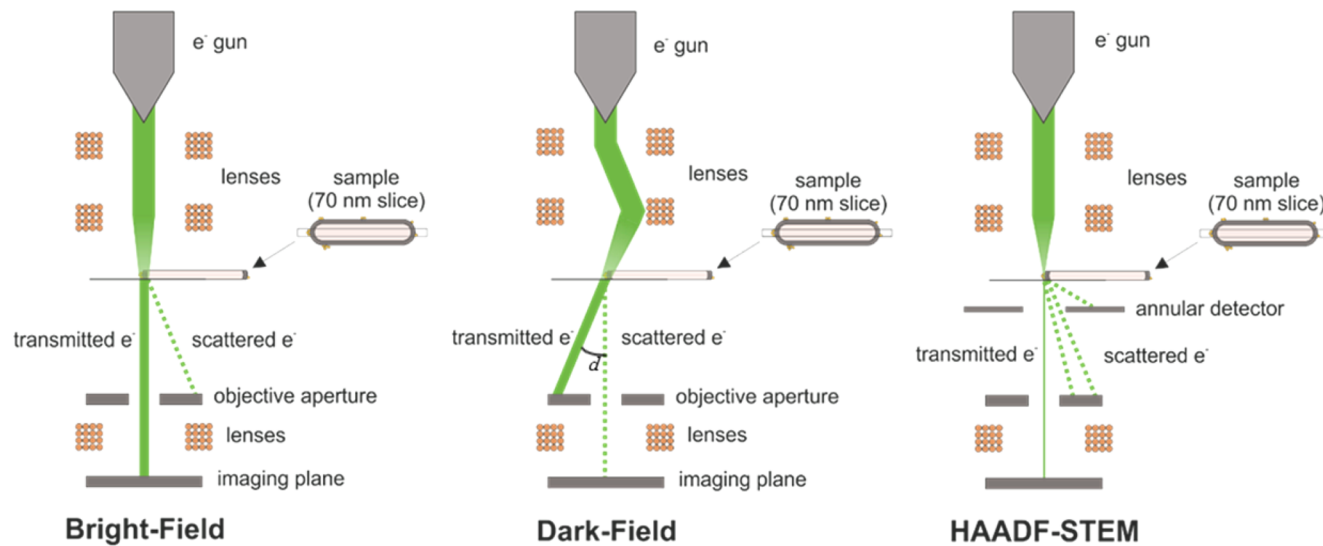


Figure 1. Comparison of bright field TEM, dark field TEM, and HAADF-STEM.

Nonbiological samples of nanoparticles were prepared for imaging on 200 mesh copper grids with Formvar and carbon supports from Ted Pella Inc. (Redding, CA) by dip coating the grid into an ethanolic solution of the nanoparticles and allowing the grid to dry in air. Dark field images were obtained by tilting the beam radially in dark field mode to position the diffraction ring of interest in the center of the objective aperture. To take enough images to cover the ring, the radius of the objective aperture (a) was determined by positioning the central diffraction spot on the edge of the aperture in dark field mode. This gave a measurement of the radius in degrees of beam tilt. The radius of the diffraction ring (d) was determined similarly in degrees of beam tilt. The two radii were then used in eq 1 to calculate the number of images needed to cover the ring, rounding up to obtain an integer number of images, n . The images were taken spaced equally around the ring, incrementing the angular tilt by $(360^\circ/n)$ for each image.

Cell Incubation with Nanoparticles. Donor-derived peripheral blood mononuclear cells (PBMCs) were cultured overnight in RPMI 1640 media containing 10% fetal bovine serum, penicillin (100 U/mL), streptomycin (100 μ g/mL), and L-glutamine (100 mmol/L) at 37 °C with 5% CO₂ in a humidified incubator. The following day, PBMCs (1×10^6 cells/mL) were activated with Dynabeads Human T-activator CD3/CD28 (Life Technologies) in the presence of IL-2 (10 ng/mL), IL-7 (50 U/mL), and β -mercaptoethanol (0.1 mM) in a 24-well plate and divided every 3 days until day 12 of culture while supplementing with fresh media. Expanded PBMCs were isolated and resuspended in regular media prior to the treatment with IONPs (0.1 mg/mL) in dimethyl sulfoxide (DMSO)-containing RPMI media (2.5×10^6 cells/mL in final concentration of 3% DMSO).³¹ Cells were incubated for 30 min at 37 °C and washed twice with phosphate-buffered saline ahead of TEM sample preparation.

Bacillus subtilis was cultured in Luria–Bertani broth overnight and exchanged via Dulbecco's PBS buffer into a HEPES buffer (2 mM HEPES, 25 mM NaCl at pH 7.4) by centrifuging at 750g for 10 min. The cell culture was then incubated with 0.5 μ g/mL, 4 nm diameter poly(allylamine hydrochloride) (MW = 15 000)-wrapped Au NPs for 10 min.

Biological Sample Preparation for TEM. Following incubation for the allotted amount of time, each biological

sample was prepared for TEM imaging via a standard process of fixation, staining, dehydration, infiltration with polymer resin, oven curing, and slicing via microtome. Samples were washed in 0.1 M sodium cacodylate buffer three times, then fixed in 2.5% gluteraldehyde in 0.1 M sodium cacodylate buffer for 1 h. The fixed cells were then washed with buffer three more times and exposed to 1% osmium tetroxide in buffer for 1 h in the dark to promote heavy metal staining of lipid membranes. The samples were rinsed with buffer three more times and then moved through a gradual process of dehydration, starting with 30% ethanol and ending with absolute ethanol (multiple rinse steps at each 30%, 50%, 70%, 80%, 90%, and 100% ethanol). Samples were exposed to three rinses of propylene oxide and then to an overnight rinse with 2:1 propylene oxide/polymer resin. That solution was replaced with two washes of 1:1 propylene oxide/resin over the next 24 h. Finally, 100% resin was added, and the sample was cured at 40 °C for 24 h and 60 °C for 48 h. Sub-100 nm slices were cut from the polymer block with a Leica EM UC6 Ultramicrotome and placed on 200 mesh copper grids with carbon and Formvar supports (Ted Pella Inc.) for imaging. Image sections were stained with uranyl acetate and lead citrate for improved bright field contrast.

Image Processing. To generate a combination of n images, all images were combined into a stack in ImageJ (National Institutes of Health). For images with significant biological noise, individual background subtractions with a rolling ball radius of 50 pixels were performed on each image prior to forming a stack. The ImageJ plugin "StackReg" with the "Rigid Body" condition was then applied on the stack to correct for small amounts of drift in the image.³² The stack was transferred back to the original images, and then, all of the images were combined using the "Image Calculator" feature with a "max" function.

Image Thresholding. Mean brightness and standard deviation of an image were determined using the "Histogram" analysis in ImageJ. Thresholds were then each applied to the image at the 3σ and the 10σ levels using the "Threshold" feature in ImageJ, resulting in two separate threshold images for each collected image field. These threshold images were then color-coded by adjusting the "Color Balance" in ImageJ to give a red color for the 3σ threshold image and a yellow color for the 10σ threshold image. For dark field composites, this process

was performed on each individual dark field image, and the resultant threshold images were combined by using the "Image Calculator" feature with the "max" function in ImageJ. To obtain a pixel count above each threshold, the appropriate composite threshold images were analyzed with the "Histogram" feature, and the pixel count at zero brightness was subtracted from the total number of pixels in the image.

RESULTS AND DISCUSSION

The utility of dark field imaging is quickly evident when examining complex biological samples. What begins as a problem of finding the needle, nanoparticles, in a haystack of biological matrix is further compounded by the difference in scale between nanomaterials and cells. To image many cells in a reasonable time, images must be taken at a low magnification where a majority of the cell is visible at once. At those scales, nanoparticles are often dwarfed by cellular structures. For example, Figure 2 demonstrates the localization of gold nanoparticles (Au NPs) following incubation with *Bacillus subtilis* bacteria as imaged in bright and dark field modes. Dark

field imaging (b, d, and f) clearly reveals the Au NPs as much brighter individual spots. While corresponding dark spots might be found in the same location in the bright field images, it is difficult to differentiate them from biological or stain artifacts of similar size that are also present. Nanoparticle clustering or aggregation at cellular membranes can be clearly observed. The state of nanoparticles upon exposure to biological systems provides important information as it affects cellular uptake and toxicity.^{33–35} Finally, it is clearly shown in both (b) and (d) that nanoparticles are not present in the interior of bacteria with intact cell walls. Other than the clusters on the thick peptidoglycan layer of bacterial walls, Au NP clusters are only found interacting with the cytoplasmic content when cell wall material is missing (see arrows). This fact becomes readily apparent when visualized in dark field mode, while bright field mode left such observations obfuscated.

Another complication to TEM imaging in biological matrices stems from staining agents such as uranyl acetate and osmium tetroxide. These stains are commonly used to visualize cellular structures in TEM,¹⁵ but they often leave artifacts that scatter electrons enough to yield similar contrast in bright field mode when compared to nanoparticles. Both imaging difficulties (size discrepancies of cells and NPs and stain artifacts) are demonstrated by Figure 3, which shows ~10 nm IONPs and stain artifacts in human peripheral blood mononuclear cells and compares their appearance in bright (a, c, and e) and dark field (b, d, and f) modes. In bright field mode, IONPs appear as minuscule black specks when operating at a magnification that allows viewing of the majority of a cell. Stain artifacts that could be mistaken as clusters of particles, highlighted by red squares, are just as obvious, if not more so, and provide ambiguity in identifying nanoparticles in the image. To address this issue, a small portion of a standard TEM grid was spotted with stock IONP suspension, and a diffraction pattern was established for that area. A thin diffraction ring associated with the iron oxide alone, as shown in the inset in (b), was chosen and then used for subsequent dark field imaging. In dark field mode, the IONPs have a bright punctate appearance against the dark background, shown in (b) and (d) even at the low magnifications necessary to image multiple cells quickly. Moreover, the stain artifacts that appeared in bright field images did not scatter electrons at the same angle as the IONP nanoparticles and therefore appeared dim in the dark field images. The IONPs could thus be identified more readily and definitively. Even at higher magnifications (e and f), dark field can be a useful tool. The dark field image reveals at least four nanoparticles in the cytosol that were not readily distinguishable in bright field.

While a single dark field image can suggest the presence of nanoparticles, it cannot conclusively prove their absence. Because only a portion of the diffraction ring is used for any given image, it only shows those nanoparticles that diffract electrons in that particular direction. Nanoparticles which are oriented to diffract in a different spot on the ring will not appear bright in the dark field image. To image a majority of the nanoparticles contributing to a diffraction ring, multiple images must be taken as the objective aperture moves around the entire ring.

Hollow-cone imaging modes address this matter by continually changing the angular tilt angle of the beam throughout image acquisition. These modes are typically only found on specialized transmission electron microscopes, however, such as those capable of STEM imaging. A similar

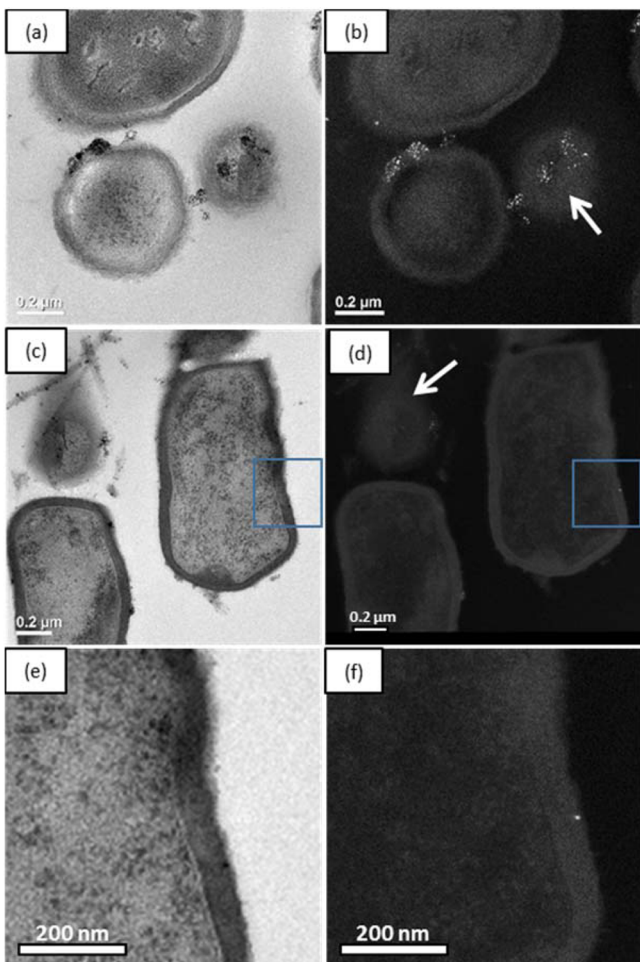


Figure 2. *B. subtilis* bacteria after incubation with 4 nm diameter Au NPs, imaged using bright field (a), (c), and (e) or dark field (b), (d), and (f) TEM. Cell content without a cell wall is indicated by arrows. A single Au NP that is clearly visible in dark field (d) but not as readily in bright field (c) is indicated by a blue box. Panels (e) and (f) show the area of the blue box at higher magnification. Panels (d) and (f) are a single image which has been adjusted with "StackReg" (also the source of the black area on the bottom of the image).

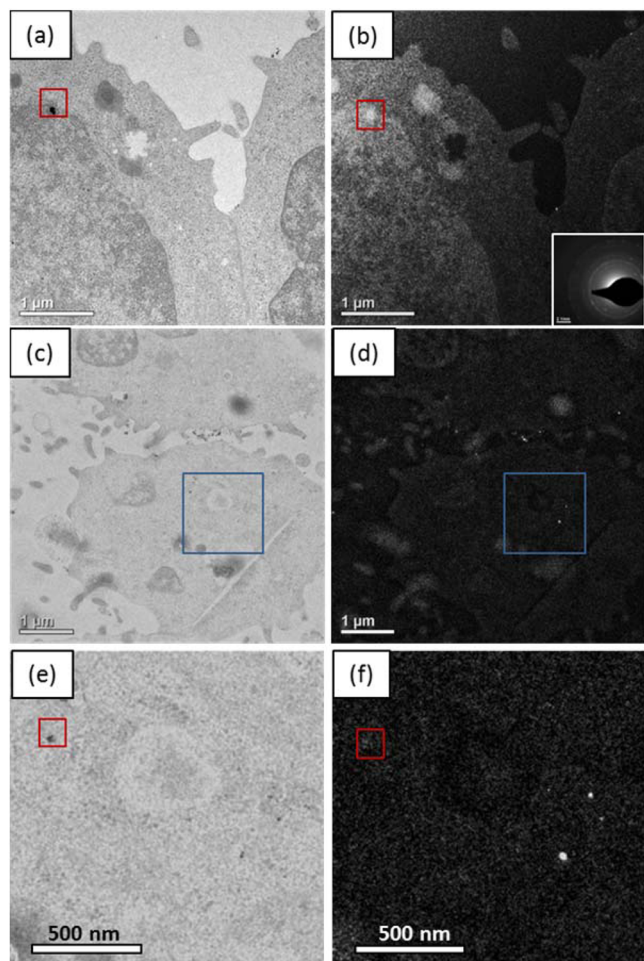


Figure 3. Human PBMCs incubated with IONPs, as they appear in bright field (a), (c), and (e) and corresponding dark field images (b), (d), (f). Cellular or stain artifacts that could be mistaken for nanoparticles in bright field mode are indicated by a red square. (e) and (f) are magnified images of the blue squares in (c) and (d). Inset: diffraction pattern from IONPs doped on the edge of the TEM grid.

result can be obtained manually as shown in Figure 4a and eq 1. By acquiring n images spaced equally around the diffraction ring, the entire ring can be captured and the resultant dark field images will display the majority of nanoparticles whose diffraction contributes to that ring (see the Supporting Information for mathematical derivation of eq 1).

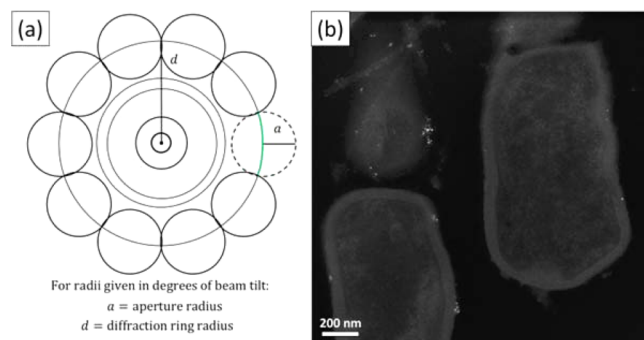


Figure 4. (a) Diagram of aperture spacing necessary to acquire images covering the entire diffraction ring. (b) Composite of n (in this case 10) images taken with the same sample from Figure 2c–f.

$$n = \left\lceil \frac{360^\circ}{2 \cos^{-1} \left(1 - \frac{(\tan a)^2}{2(\tan d)^2} \right)} \right\rceil \quad (1)$$

where n is the integer number of images required, a is the radius of the aperture in degrees beam tilt, and d is the radius of the diffraction ring in degrees beam tilt (as reported in dark field mode microscope control software).

All n images can be easily combined via the ImageJ plugin “StackReg,” which also accounts for slight stage drift during image acquisition.³² This method was applied to the same *B. subtilis* sample with Au NPs from Figure 2c–f and resulted in Figure 4b. This composite image combined 10 dark field images that were acquired, clearly demonstrating the lack of internalization of Au NPs by bacteria with intact cell walls. Because the entire diffraction ring for the Au NPs was imaged, conclusions can be more readily drawn about the absence of crystalline Au NPs inside the intact cells. See the supplemental movie, Supporting Information, for a sequence of the 10 individual images that make up this composite.

This method of image composition allows for quantification and comparison of bright and dark field images from a limit of detection (LOD, 3σ) and limit of quantitation (LOQ, 10σ) perspective. By measuring the number of pixels that are significantly different from the mean brightness for each type of image, a means of discriminating nanoparticles and visually similar structures from the remainder of the image can be obtained. For bright field images, pixels significantly darker than the mean were accounted for, while in dark field, pixels significantly brighter than the mean were used. Figure 5a shows the results of these measurements for three separate bright field images and their corresponding dark field composite images. In all of the bright field images, the standard deviation of the brightness was large enough that the 10σ threshold was below the minimum brightness. In contrast, the dark field images have a small enough standard deviation that pixels could be discriminated at varying levels of significance. By color-coding the pixels above the 3σ and 10σ thresholds, as in Figure 5b, it can be shown that the pixels above the thresholds correspond closely to the nanoparticles in the dark field composite.

Interestingly, the fact that microscopes without hollow-cone imaging require multiple images could prove to be an advantage for other applications. For example, when multidomain inorganic nanoparticles are imaged in dark field mode, various facets of the same crystallinity become visible depending on one’s position around the diffraction ring. Figure 6 demonstrates this phenomenon with 60 nm diameter commercially available Au NPs. Bright field mode displays completely black contrast due to high mass and diffraction scattering. Hollow-cone or HAADF-STEM imaging would display primarily bright nanoparticle shapes throughout. Dark field mode taken at various diffraction angles, however, reveals heterogeneous facets unseen in bright field. By acquiring data sequentially, it should be possible to glean information about crystal growth, oriented aggregation, and other parameters related to nanoparticle synthesis and particle–particle interactions.^{36,37}

CONCLUSION

We have presented the use of a known technique, dark field TEM imaging, for a new application, the facile identification and characterization of inorganic nanoparticles in biological matrices. Dark field mode provides the advantages of noise

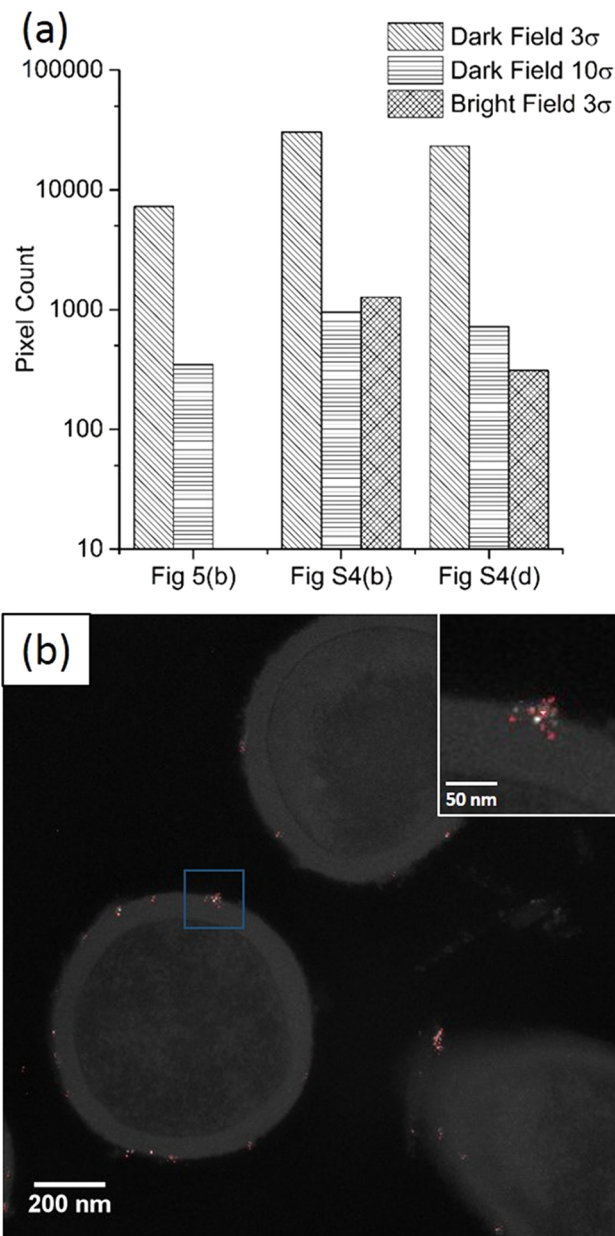


Figure 5. (a) Quantification of pixels above σ threshold brightness values in dark field and corresponding bright field images. (b) Composite dark field image with pixels above σ thresholds color-coded. Red: 3σ ; yellow: 10σ . The corresponding bright field image can be found in Figure S4e, Supporting Information. Inset: magnified image of the blue square in (b).

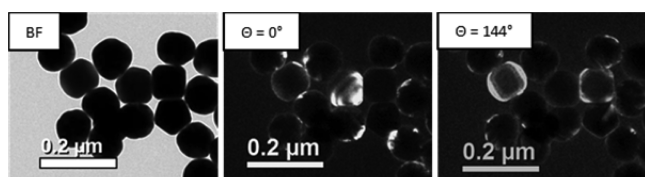


Figure 6. Images at varying angular tilts of large gold nanoparticles, demonstrating a variety of facets that appear when imaged in dark field mode.

reduction and clear nanoparticle identification via crystallinity. In addition, the visualization of nanoparticle facets via this technique could lead to new insights in fundamental nano-

particle studies. We envision that this technique will be quickly and easily adopted by researchers with an interest in quicker and more accurate studies of inorganic nanoparticles and biological systems.

ASSOCIATED CONTENT

S Supporting Information

Derivation of eq 1, analysis of the number of IONPs visible in bright and dark field images, consideration of the effect of diffraction ring thickness on imaging, and a series of dark field TEM images assembled as a movie. This material is available free of charge via the Internet at <http://pubs.acs.org>.

AUTHOR INFORMATION

Corresponding Author

*E-mail: chaynes@umn.edu.

Author Contributions

†N.D.K. and K.R.H. contributed equally.

Notes

The authors declare no competing financial interest.

ACKNOWLEDGMENTS

Parts of this work were carried out in the Characterization Facility, University of Minnesota, which receives partial support from NSF through the MRSEC program. K.R.H. acknowledges a University of Minnesota Doctoral Dissertation Fellowship for funding. N.D.K. acknowledges University of Minnesota Undergraduate Research Scholarship 11098 for funding. Z.V.F. acknowledges a Research Opportunity Award through the *Center for Sustainable Nanotechnology* (NSF CHE-1240151). Additional funding was provided by a University of Minnesota “MN Futures” seed grant. The authors wish to thank Carston Wagner and Sidath Kumarapperuma for providing PBMC samples, Lisa Jacobs, Ariane Vartarian, and Catherine J. Murphy for providing 4 nm diameter Au nanoparticles, and Fang Zhou for microtome slicing of TEM samples.

REFERENCES

- Treuel, L.; Jiang, X.; Nienhaus, G. U. *J. R. Soc. Interface* **2013**, *10*, 20120939.
- Bouwmeester, H.; Lynch, I.; Marvin, H. J.; Dawson, K. A.; Berges, M.; Braguer, D.; Byrne, H. J.; Casey, A.; Chambers, G.; Clift, M. J. *Nanotoxicology* **2011**, *5*, 1–11.
- Maurer-Jones, M. A.; Gunsolus, I. L.; Murphy, C. J.; Haynes, C. L. *Anal. Chem.* **2013**, *85*, 3036–3049.
- Shah, N. B.; Dong, J.; Bischof, J. C. *Mol. Pharmaceutics* **2011**, *8*, 176–184.
- Lamprecht, C.; Gierlinger, N.; Heister, E.; Unterauer, B.; Plochberger, B.; Brameshuber, M.; Hinterdorfer, P.; Hild, S.; Ebner, A. *J. Phys.: Condens. Matter* **2012**, *24*, 164206.
- Perevedentseva, E.; Hong, S.-F.; Huang, K.-J.; Chiang, I.-T.; Lee, C.-Y.; Tseng, Y.-T.; Cheng, C.-L. *J. Nanopart. Res.* **2013**, *15*, 1–12.
- Yang, P.-H.; Sun, X.; Chiu, J.-F.; Sun, H.; He, Q.-Y. *Bioconjugate Chem.* **2005**, *16*, 494–496.
- Lapotko, D. O.; Lukianova, E. Y.; Chizhik, S. A. *Proc. SPIE* **2007**, *6447*, 644703 DOI: 10.1117/12.712855.
- Tetard, L.; Passian, A.; Farahi, R. H.; Voy, B. H.; Thundat, T. In *Nanotoxicity*; Springer: New York, 2012; pp 331–343.
- Tetard, L.; Passian, A.; Thundat, T. *Nat. Nanotechnol.* **2009**, *5*, 105–109.
- Tetard, L.; Passian, A.; Farahi, R. H.; Thundat, T. *Ultramicroscopy* **2010**, *110*, 586–591.
- Shen, H.; Long, D.; Zhu, L.; Li, X.; Dong, Y.; Jia, N.; Zhou, H.; Xin, X.; Sun, Y. *Biophys. Chem.* **2006**, *122*, 1–4.

- (13) Zhang, Y.; Yang, M.; Ozkan, M.; Ozkan, C. S. *Biotechnol. Prog.* **2009**, *25*, 923–928.
- (14) Mayhew, T. M.; Mühlfeld, C.; Vanhecke, D.; Ochs, M. *Ann. Anat.* **2009**, *191*, 153–170.
- (15) Schrand, A. M.; Schlager, J. J.; Dai, L.; Hussain, S. M. *Nat. Protoc.* **2010**, *5*, 744–757.
- (16) Ayache, J.; Beaunier, L.; Boumendil, J.; Ehret, G.; Laub, D. In *Sample Preparation Handbook for Transmission Electron Microscopy*; Springer: New York, 2010; pp 125–170.
- (17) Morones, J. R.; Elechiguerra, J. L.; Camacho, A.; Holt, K.; Kouri, J. B.; Ramírez, J. T.; Yacaman, M. J. *Nanotechnology* **2005**, *16*, 2346.
- (18) Chamakura, K.; Perez-Ballesteros, R.; Luo, Z.; Bashir, S.; Liu, J. *Colloids Surf., B* **2011**, *84*, 88–96.
- (19) Dahmen, T.; Baudoin, J.-P.; Lupini, A. R.; Kübel, C.; Slusallek, P.; de Jonge, N. *Microsc. Microanal.* **2014**, *20*, 548–560.
- (20) Roose, D.; Leroux, F.; De Vocht, N.; Guglielmetti, C.; Pintelon, I.; Adriaensen, D.; Ponsaerts, P.; Van der Linden, A.; Bals, S. *Contrast Media Mol. Imaging* **2014**, *9*, 400–408.
- (21) Landis, W. J.; Glimcher, M. J. *J. Ultrastruct. Res.* **1982**, *78*, 227–268.
- (22) Schultz, T. W.; Freeman, S. R.; Dumont, J. N. *Arch. Environ. Contam. Toxicol.* **1980**, *9*, 23–40.
- (23) Kawahara, I.; Koide, M.; Tadokoro, O.; Udagawa, N.; Nakamura, H.; Takahashi, N.; Ozawa, H. *Bone* **2009**, *45*, 980–986.
- (24) Ferin, J.; Coleman, J. R.; Davis, S.; Morehouse, B. *Arch. Environ. Health* **1976**, *31*, 113–115.
- (25) Ponce, A.; Mejía-Rosales, S.; José-Yacamán, M. In *Nanoparticles in Biology and Medicine*; Springer: New York, 2012; pp 453–471.
- (26) Sousa, A. A.; Leapman, R. D. *Ultramicroscopy* **2012**, *123*, 38–49.
- (27) Aronova, M. A.; Leapman, R. D. *MRS Bull.* **2012**, *37*, 53–62.
- (28) Murphy, C. J.; Gole, A. M.; Stone, J. W.; Sisco, P. N.; Alkilany, A. M.; Goldsmith, E. C.; Baxter, S. C. *Acc. Chem. Res.* **2008**, *41*, 1721–1730.
- (29) Liu, M.; Chao, J.; Deng, S.; Wang, K.; Li, K.; Fan, C. *Colloids Surf., B* **2014**, *124*, 111–117.
- (30) De Jonge, N.; Ross, F. M. *Nat. Nanotechnol.* **2011**, *6*, 695–704.
- (31) Bhatnagar, P.; Alauddin, M.; Bankson, J. A.; Kirui, D.; Seifi, P.; Huls, H.; Lee, D. A.; Babakhani, A.; Ferrari, M.; Li, K. C.; Cooper, L. J. *Sci. Rep.* **2014**, *4*, 4502.
- (32) Thevenaz, P.; Ruttimann, U. E.; Unser, M. *IEEE Trans. Image Process.* **1998**, *7*, 27–41.
- (33) Albanese, A.; Tang, P. S.; Chan, W. C. *Annu. Rev. Biomed. Eng.* **2012**, *14*, 1–16.
- (34) Albanese, A.; Chan, W. C. *ACS Nano* **2011**, *5*, 5478–5489.
- (35) Braydich-Stolle, L. K.; Breitner, E. K.; Comfort, K. K.; Schlager, J. J.; Hussain, S. M. *Langmuir* **2014**, *30*, 15309–15316.
- (36) Bahrig, L.; Hickey, S. G.; Eychmüller, A. *CrystEngComm* **2014**, *16*, 9408–9424.
- (37) Xue, X.; Penn, R. L.; Leite, E. R.; Huang, F.; Lin, Z. *CrystEngComm* **2014**, *16*, 1419–1429.